Letter

Superradiance decoherence caused by long-range Rydberg-atom pair interactions

Elmer Suarez , Philip Wolf, Patrizia Weiss , and Sebastian Slama *

Center for Quantum Science and Physikalisches Institut,
Eberhard-Karls Universität Tübingen, Auf der Morgenstelle 14, 72076 Tübingen, Germany

This Research Letter reports on the observation of superradiance decoherence caused by long-range dipole-dipole interactions between Rydberg atoms. A cold atom cloud is prepared in the mode volume of a weakly driven optical cavity and excited to a Rydberg state. The cavity transmission monitors the Rydberg dynamics in real time and detects superradiant enhancement of the transition rates between neighboring Rydberg states. The observed enhancement is reduced for increasing Rydberg atom density: a signature of atom pair interactions. The observations are explained within a model based on the idea of Rydberg blockade reducing the atom number participating in the Dicke state, responsible for superradiance.

I. INTRODUCTION

Rydberg atoms offer important prospects for realizing quantum gates [1,2], quantum memories [3], single-photon devices [4,5], and long-range interacting many-body quantum systems [6]. A key step is the efficient coherent excitation of Rydberg atoms [7,8]. At room temperature, black-body radiation (BBR) couples neighboring Rydberg states. As a result, the coherent excitation of Rydberg atoms is spread over several states [9]. Furthermore, superradiance (SR) can lead to a speedup of this process as observed with atomic beams in a superconducting microwave cavity [10] or triggered in free space by a weak microwave pulse [11]. Nonetheless, BBR-induced superradiance in clouds of cold atoms has been controversially discussed in the Rydberg community, as some experiments have reported its direct or indirect observation [12–15], whereas others have reported its absence [16]. Atomic interactions, already known to lead to line broadening of Rydberg states [17,18], also offer a possible explanation of superradiance suppression. In particular, a recent theoretical work [19] has shed light on the debate by considering the influence of dephasing, induced by dipole-dipole interactions, on superradiance, and the competition between superradiant transitions.

This Research Letter experimentally addresses the question of why superradiance is observed in some cold Rydberg experiments and not in some others. It investigates the influence of dipole-dipole interactions on superradiance by tracking the time dynamics of a Rydberg state for various Rydberg atom densities. It turns out that superradiant enhancement is favored by more dilute atom clouds. In order to explain the observations, a model based on the idea of Rydberg blockade is introduced [Fig. 1]. The conclusions from this Research Letter reconcile the former contradicting observations.

II. REAL-TIME DETECTION OF RYDBERG DYNAMICS

An optical cavity is used as a real-time detector of the Rydberg dynamics [Fig. 2(a)]. This method extends recent work where optical cavities have been used as real-time monitors for the expansion of an atomic cloud [20], for a dynamical phase transition [21], and for evaporative cooling [22]. A complementary approach using a superconducting microwave cavity has been recently demonstrated for counting Rydberg atoms [23]. Real-time detection of a two-photon Rydberg excitation has also been realized in hot vapor cells [24,25]. In this Research Letter, cold ^{87}Rb atoms interact with the optical cavity in the collective strong-coupling regime [26], i.e., featuring a collective normal mode splitting [Fig. 2(b)]. Then, the transmission on the side of the fringe of one of the normal modes depends on the number of atoms interacting with the cavity. Since Rydberg atoms cannot interact with the cavity, as it is near resonant only with the lower transition shown in Fig. 2(c), the transmission probes the internal state dynamics of the atoms in real time, while they are pumped to a Rydberg state. This allows us to detect and quantify also superradiant decay from the Rydberg state to neighboring states.

III. EXPERIMENTAL SETUP

In the experiment, ^{87}Rb atoms are laser cooled in a magneto-optical trap (MOT) overlapped with a confocal cavity of 50 mm length and full width at half maximum $\nu_{\text{FWHM}} = 13.4$ MHz, corresponding to a finesse $F = 224$. The single atom-cavity coupling is $g_0 = 2\pi \times 206.8$ kHz. The cavity length is controlled with a piezoelectric transducer (piezo) by stabilizing it to a far-detuned external cavity diode laser (ECDL) using the Pound-Drever-Hall technique, i.e., the lock laser with 786 nm wavelength. The lock laser itself is stabilized to a high-finesse reference cavity. Light from another ECDL is divided into two beams: the probe beam (frequency ω_p) probes the atom-cavity system, and the pump beam (frequency ω_1) drives the $5S_{1/2}$-to-$5P_{3/2}$ transition with Rabi

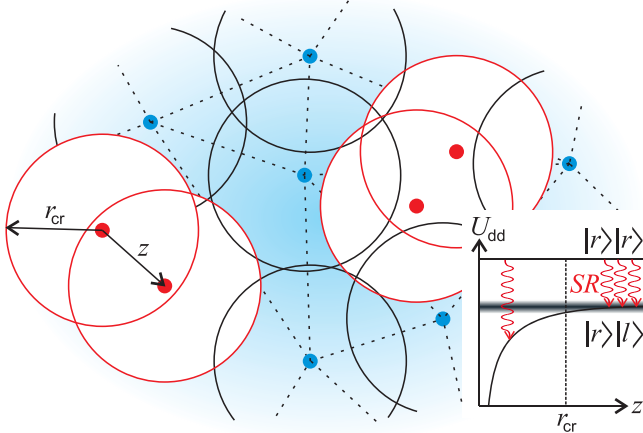*sebastian.slama@uni-tuebingen.de

L041302-1

FIG. 1. Representation of a set of interacting Rydberg atoms. Superradiant decay from state $|r\rangle$ to a neighboring Rydberg state $|l\rangle$ is possible as long as they form a coherent many-body state: a Dicke state (in blue, dashed lines, shaded region). If the distance z to the next neighbor is smaller than the critical radius r_{cr} (in red, unshaded) the transition is tuned out of resonance due to the dipole-dipole interaction potential $U_{dd}(z)$ making those atoms unable to link to the Dicke state. Effectively, fewer atoms take part in the superradiant decay.

frequency Ω_1 [see Fig. 2(a)]. Each beam is activated by different acousto-optic modulators (AOMs), allowing for a relative detuning between them. Both beams are coupled into the cavity with linear (perpendicular) polarizations and excite different transverse modes of the cavity. Then, in order to detect probe light in transmission only, an interference filter together with an optical single-mode fiber is used. This fiber is connected to an avalanche photodiode (APD) with 10 MHz bandwidth that detects time tracks of the transmitted probe light power delivering atom-cavity spectra as in Fig. 2(b) and information on the internal state dynamics as in Fig. 3. Excitation of atoms to the Rydberg state is achieved in a two-photon process using the pump light field and a coupling light field (frequency ω_2) at 480 nm wavelength coupling the intermediate $5P_{3/2}$ state to the $30D_{5/2}$ state with Rabi frequency Ω_2. Both beams counterpropagate along a direction transverse to the cavity axis and share the same linear polarization with the probe field: perpendicular to the plane given by the cavity axis and the propagation direction. Their beam waists are $\omega_z \sim 700\ \mu$m along the cavity axis and $\omega_r \sim 125\ \mu$m perpendicular to it in order to match the density profile of the atoms in the cavity mode. The coupling light field is generated by frequency-doubling a 960-nm amplified ECDL using a lithium triborate (LBO) crystal inside a homemade bow-tie cavity. The frequency of this laser is controlled by electromagnetically induced transparency (EIT) in a Rb cell, and its power (120 mW maximum) is controlled with an AOM. The MOT laser beams are switched off during the measurements such that the atom cloud is freely expanding.

IV. ATOM-CAVITY SYSTEM

The atom-cavity system is well described by a widely used set of Maxwell-Bloch equations under the semiclassical
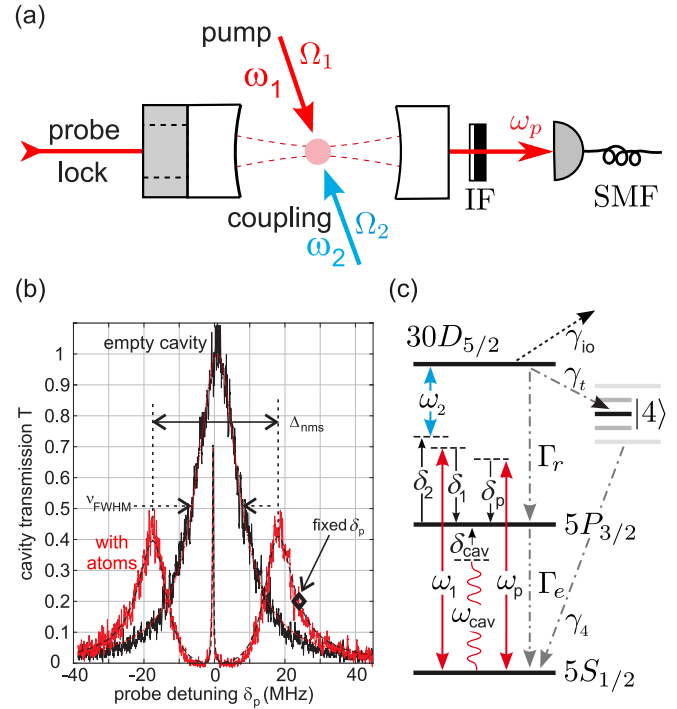

FIG. 2. (a) Experimental setup. The pump and coupling laser beams counterpropagate transversely to the cavity axis performing two-photon Rydberg excitation. Rydberg dynamics is tracked by weakly driving the cavity and monitoring its transmission with an APD. An interference filter (IF) and a single-mode fiber (SMF) filter out the 786-nm lock laser used to control the cavity length. (b) The probe laser frequency ω_p is scanned over the atom-cavity resonance, with cavity resonance ω_{cav} tuned to the atomic transition frequency. The measured empty cavity resonance is used to fit the cavity linewidth ν_{FWHM}. With atoms inside the cavity, normal mode splitting Δ_{nms} and cavity Rydberg EIT are observed and fitted in order to benchmark the system. (c) Atomic levels, laser frequencies, and decay rates involved in the Rydberg excitation. Positive and negative detunings are indicated by $\downarrow$ and $\uparrow$, respectively.

approximation [27]. In this Research Letter, the weak-probe limit is a good approximation to derive the steady-state equations. Of main interest is the normalized intracavity photon number (i.e., the cavity transmission) given by

$$T = \left| \frac{1}{1 + i(\Delta - 2C_1 N_{\text{eff}} \chi)} \right|^2, \quad (1)$$

where $\Delta = 2(\delta_{cav} - \delta_p)/\kappa$ and $C_1 = 2g_0^2/\kappa\Gamma_e$ with κ being the cavity field decay rate and Γ_e being the inverse lifetime of the $5P_{3/2}$ state. The detunings δ_{cav} and δ_p are that of the cavity and probe field relative to the atomic resonance, respectively. N_{eff} is the effective number of atoms interacting with the standing wave pattern of the cavity mode [26]. The factor $\chi = i/(1 - i2\delta_p/\Gamma_e)$ is proportional to the atomic susceptibility. By scanning the probe field frequency the atom-cavity spectrum is obtained in transmission [Fig. 2(b)]. The empty cavity resonance is fitted using Eq. (1) to measure the cavity linewidth ν_{FWHM}. Enough atoms are loaded for the spectrum to exhibit a normal mode splitting: The cavity resonance splits into two smaller peaks with a frequency difference given by $\Delta_{nms} = 2g_0\sqrt{N_{\text{eff}}}$, valid for $\delta_{cav} \ll \Delta_{nms}$. Again, with Eq. (1)
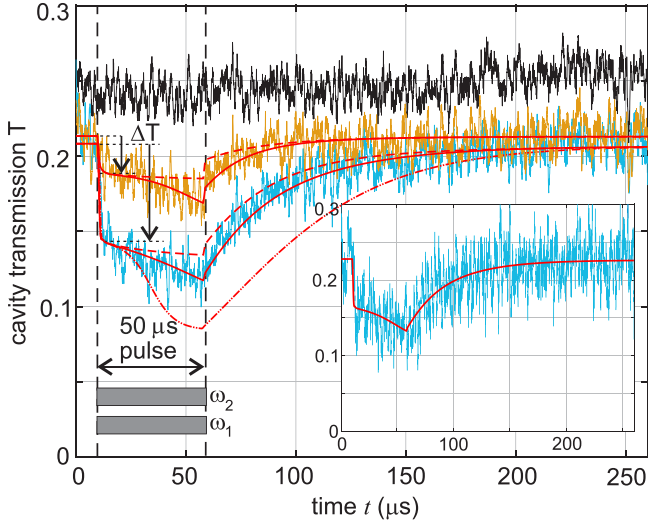
FIG. 3. Resulting time signals from monitoring the cavity transmission. Main plot: averaged data over ten repetitions of the experiment. Inset: a single (real-time) measurement. The coupling field Rabi frequency is kept fixed at $\Omega_2 = 2\pi \times 7.6$ MHz while increasing $\Omega_1 = 2\pi \times 0.9$ MHz (orange, in the middle) up to $\Omega_1 = 2\pi \times 2.9$ MHz (blue, lower curve). The black curve at the top corresponds to $\Omega_1 = 2\pi \times 2.9$ MHz and $\Omega_2 = 0$ and is vertically shifted ($+0.05$) for clarity. The solid and dashed red lines are simulations with and without superradiance, respectively. The red dash-dotted line is simulated with reduction factors $\beta_{1,2}$ taken from the fit of the orange curve. The slow decrease of the dashed lines during the pulse corresponds to shelving of the atoms due to BBR-induced transitions. Small jumps observed in the simulations at the end of the pulse are due to the fact that the coupling laser modifies the steady state of the atom-cavity system.

the effective atom number in the cavity is derived to be $N_{\mathrm{eff}} = 6.5(2) \times 10^3$. When the coupling laser is on during the recording of the spectrum, an additional narrow feature appears, i.e., cavity Rydberg EIT. This is described by a modified susceptibility of the probed transition:

$$\chi' = \frac{i}{1 - i2\delta_p/\Gamma_e + \frac{\Omega_2^2/\gamma_R \Gamma_e}{1 - i2\delta_{\mathrm{eit}}/\gamma_R}}, \qquad (2)$$

replacing the χ in (1). Here, we introduce a broadened linewidth $\gamma_R = \Gamma_r + \gamma_d$, where $\Gamma_R = 2\pi \times 8.3$ kHz is the natural linewidth of the Rydberg state and γ_d accounts for inhomogeneous broadening mainly caused by stray electric and magnetic fields, as well as by laser noise. With the definition of the EIT detuning $\delta_{\mathrm{eit}} = \delta_p + \delta_2$, the condition $\delta_{\mathrm{eit}} = 0$ corresponds to the cavity Rydberg EIT resonance [28–30]. Here, following Ref. [30], we use cavity Rydberg EIT with $\delta_2 = 0$ to benchmark our system and get values of $\Omega_2 = 2\pi \times 7.6$ MHz and $\gamma_R = 2\pi \times 650$ kHz.

V. TRACKING RYDBERG DYNAMICS

We will now describe the Rydberg excitation. The Hamiltonian for the closed three-level system interacting with two classical beams [Fig. 2(c) with $\gamma_{io,t,4} = 0$] leads to well-known three-level Bloch equations [31], which we use to simulate the dynamics of the three levels. However, note

that for large detuning δ_1, the intermediate state can be adiabatically eliminated, leading to an effective two-level system [32]. In this context, and fulfilling the two-photon resonance condition $\delta_1 = -\delta_2$, an effective Rabi frequency $\Omega_{\mathrm{eff}} = \Omega_1 \Omega_2 / 2\delta_1$ and detuning $\delta_{\mathrm{eff}} = (\Omega_1^2 - \Omega_2^2)/4\delta_1$ are introduced. The parameters for exciting Rydberg atoms in the present experiment are as follows: $\delta_1 = -\delta_2 = 2\pi \times 31.8$ MHz, $\Omega_2 = 2\pi \times 7.6$ MHz, and Ω_1 is varied with a maximum value of $\Omega_1 = 2\pi \times 3.9$ MHz, corresponding to $\Omega_{\mathrm{eff}} = 2\pi \times 350$ kHz, slightly smaller than the broadened linewidth of $\gamma_R = 2\pi \times 650$ kHz. As a result, the atomic three-level system reaches its steady state on a timescale of $2\ \mu$s, much longer than what it takes for the atom-cavity system to reach its steady state (on the order of 200 ns). Therefore the cavity field adiabatically follows the Rydberg dynamics.

From the point of view of the atom-cavity system, Rydberg excitation can be considered as atom loss. Intuitively, a Rydberg atom is unable to absorb or emit cavity photons. Thus Rydberg dynamics is introduced into Eq. (1) by making the change $N_{\mathrm{eff}} \to N_{\mathrm{eff}} P$, where $P = P_e + P_g$ is the time-dependent probability of an atom to be either in the excited state or in the ground state. Consequently, the normal mode splitting Δ_{nms} follows the time evolution of P. To observe the change in Δ_{nms}, the probe detuning is fixed at $\delta_p = +24$ MHz on the side of the fringe of one of the normal modes [Fig. 2(b)], while the cavity transmission is monitored. The resulting time signals are shown in Fig. 3 after performing a moving average over bins of $0.9\ \mu$s length.

Rydberg excitation is accomplished by a pulse of the transverse beams with $50\ \mu$s length, starting at $t = 10\ \mu$s. Before the pulse, the signal corresponds to the steady state of the atom-cavity system. This piece of the signal is used to determine a value for δ_{cav}, which together with the atom number (determined independently from the normal mode spectrum) is assumed to be constant for the full length of the signal. It turns out that technical atom number shot-to-shot variations do not influence the dynamics substantially. The step ΔT in the transmission signal at the beginning of the pulse corresponds to the coherent Rydberg excitation. Rabi oscillations are not observed due to the large dephasing rate γ_d. An increasing Ω_1 leads to a larger Ω_{eff} and a smaller δ_{eff}, and thus to a larger production of Rydberg atoms. This is observed in Fig. 3 as an increased step in the blue data compared with the orange data. A closed three-level system would have reached its steady state after this step. The measurements, instead, show a slower but continuous decrease even after ΔT. Since the signal goes back to its initial value after the end of the laser pulse, the slow decrease cannot be due to the loss of atoms out of the cavity, for instance caused by the expansion of the cloud. Furthermore, by setting $\Omega_2 = 0$ and Ω_1 to its maximum value, a constant signal is observed (black data), showing that light scattering of the pump laser does not contribute to the observed behavior.

VI. BBR-INDUCED TRANSITIONS AND SR

The slow decrease observed in Fig. 3 during the pulse can be explained by BBR-induced transitions. Here, atoms decay from the initial Rydberg state to long-lived neighboring Rydberg states, where they are shelved [13,14,16]. For this,

various decay channels from the $30D_{5/2}$ state are described with a set of rate equations

$$\dot{\vec{N}} = A\vec{N}. \qquad (3)$$

Here, $\vec{N}$ is a vector containing the populations of all states considered, and A is a matrix containing the transition rates coupling them. The Alkali Rydberg Calculator (ARC) [33] is used to build the matrix A including spontaneous decay transitions (to and beyond $5P_{3/2}$) and BBR-induced transitions from $30D_{5/2}$ and its closest neighbors. An ionization loss rate of $\gamma_{io} = 500$ Hz [34] is also included, but negligible compared with the other rates. The rate equations (3) are solved together with the Bloch equations of the three-level system, to obtain $P(t)$ and, using Eqs. (1) and (2), the time evolution of the cavity transmission. The results are plotted as red dashed lines in Fig. 3. They qualitatively agree with the experimental curves but do not fully explain the observed slow decrease quantitatively.

Instead, the curves suggest a speedup of the shelving process. We attribute this speedup to superradiance [35]. SR is particularly influenced by the atomic system geometry: It is favored by situations when its transition wavelength is larger than the size of the ensemble. This is gauged by the cooperativity parameter [14]

$$C_{rl} = \frac{9(\sin(k_{rl}R) - k_{rl}R\cos(k_{rl}R))^2}{(k_{rl}R)^6}, \qquad (4)$$

valid for an ideal spherical atomic cloud of homogeneous density and radius R, where k_{rl} is the wave number for the transition from state r to state l. For the initial $30D_{5/2}$ Rydberg state and a MOT radius of $R = 0.5$ mm, two final states are identified for featuring a superradiant decay: $31P_{3/2}$ and $28F_{7/2}$. We verified theoretically that BBR decay is almost exclusively concentrated in these decay channels. The corresponding transition wavelengths are 3.6 and 1.5 mm, while the transition rates including BBR from $30D_{5/2}$ to $31P_{3/2}$ and $28F_{7/2}$ are 1.7 and 4.1 kHz, respectively. Superradiant decay is included in the rate Eqs. (3) by adding a nonlinear term:

$$\frac{dN_{r,l}}{dt} = \mp\Gamma_{rl}C_{rl}\beta_{rl}N_r(N_l + 1), \qquad (5)$$

where $N_{r,l}$ is the number of atoms in state r, l and Γ_{rl} is the BBR-induced transition rate. The factor β_{rl} describes the action of decoherence and is introduced in the following model.

VII. DECOHERENCE MODEL

SR is based on the emission of photons by a collection of indistinguishable atoms (it is unknown which atom has emitted a given photon). This leads to the buildup of an extended coherent many-body state, i.e., the Dicke state. The Dicke state is susceptible to dephasing due to inhomogeneities in the transition energies across the sample [36]. A rigorous theoretical method to include dipole-dipole interactions in superradiant systems is presented in Ref. [19], where dipole-dipole interactions are introduced in the master equation, which is then numerically solved after truncation of higher-order correlations. We introduce here a simpler model based on the idea of Rydberg blockade [37]. Given the Rydberg densities of our experiment, it is well justified to neglect the $1/r^6$ van der Waals interaction between two atoms in equal
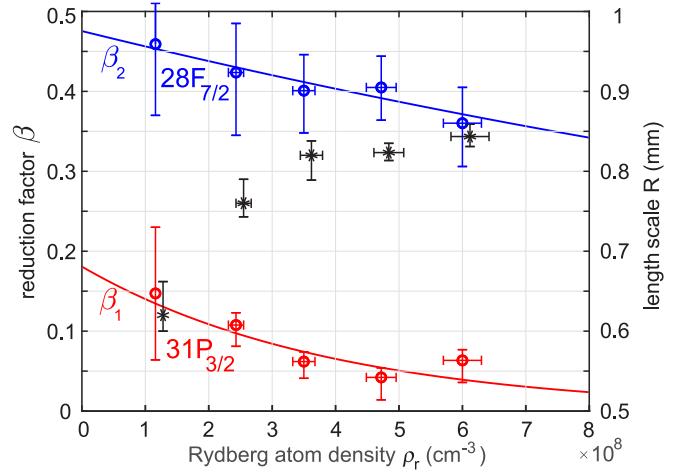

FIG. 4. Obtained parameters after fitting time signals as in Fig. 3. Circles (left axis) denote the reduction factors β_1 and β_2 for the two superradiant decays down to the $31P_{3/2}$ and $28F_{7/2}$ states, respectively. Stars (right axis) denote the length scale R of the superradiant cloud. Vertical error bars represent a 95% confidence interval, and horizontal error bars represent a 5% uncertainty in the atom number. Solid lines are exponential fits [Eq. (7)] to the reduction factor's dependence on Rydberg atom density ρ_r. Data for R are shifted to the right by one data width for clarity.

Rydberg states. However, the transition of one of the atoms to a neighboring Rydberg state experiences an additional interaction shift by the $1/r^3$ dipole-dipole interaction. If the interaction shift is larger than the broadened linewidth of the transition, given by an interatomic distance smaller than the critical radius (i.e., the blockade radius), the atom pair is distinguishable from the rest of the atoms and cannot participate in the Dicke state [Fig. 1]. Essentially, the number of atoms N_r participating in the superradiant transition is reduced. We account for this reduction of atoms in the simulations by introducing factors $\beta_{1,2} < 1$ in (5) for the two superradiant transitions that we consider. These factors are fitted to the measured curves, together with the cloud size R that enters (5) via (4). We obtain the red solid lines in Fig. 3. Those exhibit a speedup of the shelving process and quantitatively fit to the measurements. We include also a simulation based on the parameters of the blue data, but with $\beta_{1,2}$ taken from the fit of the orange data (red dash-dotted line). It clearly deviates from the blue data, confirming that the reduction factor is different for each curve.

Long-range dipole-dipole interactions between Rydberg atoms, unlike inhomogeneous electric or magnetic fields, introduce a dephasing that strongly depends on the distance between the atoms. Thus, in order to investigate their role in SR, we record time signals for different values of Ω_1 and plot the fitted parameters β_1, β_2, and R in Fig. 4 as a function of the corresponding Rydberg atom density $\rho_r = P_r\rho$. Here, P_r is the steady-state probability for an atom in the closed three-level system to be in the Rydberg state. The reduction factors in Fig. 4 show that superradiance is suppressed for growing Rydberg atom density. This observation proves that atomic interactions are responsible for this effect. The functional dependence that we expect for β_{rl} is given by the probability that

the nearest neighbor of a Rydberg atom is outside a spherical volume of radius r_{cr}:

$$p(\rho_r, r_{cr}) = e^{-\frac{4\pi}{3}\rho_r r_{cr}^3}. \qquad (6)$$

Thus the atom number participating in SR is reduced to $p(\rho_r, r_{cr})N_r$. Following Eq. (5), the experimentally determined values of $\beta_{1,2}$ in Fig. 4 are fitted with an exponentially decaying function

$$\beta_{1,2} = A_{1,2} e^{-\frac{4\pi}{3}\rho_r r_{cr,1,2}^3}, \qquad (7)$$

resulting in experimentally determined values for the critical radii of $r_{cr,1} = (8.4 \pm {}^{1.4}_{1.6})$ μm and $r_{cr,2} = (4.6 \pm {}^{1.0}_{1.9})$ μm. Uncertainties are based on the 1σ confidence interval of the fit. Equation (7) includes also constant prefactors $A_{1,2}$ to incorporate a further reduction of superradiant atoms for each transition, with fitted values of $A_1 = 0.18 \pm {}^{0.09}_{0.07}$ and $A_1 = 0.48 \pm {}^{0.06}_{0.07}$. This kind of reduction is density independent and is thus not caused by atom pair interactions.

We estimate theoretical values for the critical radii to compare them with the experimental results. The critical radius is defined by the distance where the dipole-dipole potential strength $U_{dd} = C_3/z^3$ equals the linewidth of the transition, which we assume to be identical to the broadened linewidth γ_R of the initial $30D_{5/2}$ Rydberg state, resulting in

$$r_{cr,k} = \sqrt[3]{\langle C_{3,k}\rangle/\gamma_R}. \qquad (8)$$

Here, $\langle C_{3,k}\rangle$ denotes an average over the $C_{3,k}^{j,j'}$ coefficients of the dipole-allowed transitions from the m_j sublevels of $30D_{5/2}$ down to the m_j' sublevels of state $|k\rangle$:

$$\langle C_{3,k}\rangle = \frac{1}{n_j} \sum_{j' \neq j} C_{3,k}^{j,j'} G_{j,j'}^2, \qquad (9)$$

which are weighted with the squared Clebsch-Gordan coefficients $G_{j,j'}^2$ of the corresponding transitions. The values of $C_{3,k}^{j,j'}$ and $G_{j,j'}$ are taken from Ref. [33]. The normalization factor $n_j = \sum_{j,j'} G_{j,j'}^2$ equals the number of m_j sublevels. In addition, we average also over the angle dependence of the dipole-dipole potential $\propto |1 - 3\cos^2\theta|$ [38], with angle θ between the quantization axis and the internuclear axis. The modulus is included in order not to balance positive frequency shifts with negative ones, as both signs lead to a detuning from the superradiant transition. Thus we derive values of $r_{cr,1}^{th} = 7.9$ μm and $r_{cr,2}^{th} = 5.4$ μm, respectively. They agree with the experimentally determined values within their uncertainties.

The observed reduction of the length scale R for decreasing ρ_r in Fig. 4 is explained by the Gaussian spatial profile of $\Omega_{1,2} \propto \exp(-r^2/w_0^2)$ with $1/e$ beam radius w_0, together with the nonlinear dependence of the Rydberg atom density on the Rabi frequency. For weak driving, it scales as $\rho_r \propto \Omega_1^2$. Thus

the $1/e$ radius of the Rydberg cloud is given by $r_0 = w_0/\sqrt{2}$. As the peak Rabi frequency is increased (but still below saturation), Rydberg excitation scales linearly as $\rho_r \propto \Omega_1$. In this case, cloud radius and beam radius are equal: $r_0 = w_0$. The factor of $\sqrt{2}$ difference in r_0 matches the observation in Fig. 4.

VIII. CONCLUSION

In conclusion, based on the atom number dependence of the collective atom-cavity coupling, a method has been introduced to track Rydberg dynamics in real time. The method has been used to detect the excitation of rubidium atoms to the $30D_{5/2}$ state and their BBR-induced decay to neighboring Rydberg levels. The measurements are quantitatively explained by a model that includes superradiance to two adjacent levels and, in particular, decoherence, which effectively lowers the number of superradiant atoms. The observed decoherence depends on the Rydberg atom density in a way that is consistent with long-range dipole-dipole interactions between an atom in the initial Rydberg state and an atom in the final Rydberg state. These results reconcile previously reported contradicting observations: The observation of superradiance in the decay to neighboring Rydberg states requires, on one hand, sufficiently large numbers of Rydberg atoms for enhancement. This is the reason why superradiance is elusive in experiments with few atoms. On the other hand, it requires low enough densities to avoid dipole-dipole interactions. Our experiment with a dilute MOT operates just in the right density range to probe the growing influence of dipole-dipole interactions. A further perspective is to investigate competition between different superradiant decay channels.

[1] T. Wilk, A. Gaëtan, C. Evellin, J. Wolters, Y. Miroshnychenko, P. Grangier, and A. Browaeys, Entanglement of Two Individual Neutral Atoms Using Rydberg Blockade, Phys. Rev. Lett. **104**, 010502 (2010).

[2] L. Isenhower, E. Urban, X. L. Zhang, A. T. Gill, T. Henage, T. A. Johnson, T. G. Walker, and M. Saffman, Demonstration of a Neutral Atom Controlled-NOT Quantum Gate, Phys. Rev. Lett. **104**, 010503 (2010).

[3] L. Li and A. Kuzmich, Quantum memory with strong and controllable Rydberg-level interactions, Nat. Commun. **7**, 13618 (2016).

[4] H. Gorniaczyk, C. Tresp, J. Schmidt, H. Fedder, and S. Hofferberth, Single-Photon Transistor Mediated by Interstate Rydberg Interactions, Phys. Rev. Lett. **113**, 053601 (2014).

[5] D. Tiarks, S. Baur, K. Schneider, S. Dürr, and G. Rempe, Single-Photon Transistor Using a

Förster Resonance, Phys. Rev. Lett. **113**, 053602 (2014).

[6] P. Schauß, J. Zeiher, T. Fukuhara, S. Hild, M. Cheneau, T. Macri, T. Pohl, I. Bloch, and C. Gross, Crystallization in Ising quantum magnets, Science **347**, 1455 (2015).

[7] T. Cubel, B. K. Teo, V. S. Malinovsky, J. R. Guest, A. Reinhard, B. Knuffman, P. R. Berman, and G. Raithel, Coherent population transfer of ground-state atoms into Rydberg states, Phys. Rev. A **72**, 023405 (2005).

[8] J. Deiglmayr, M. Reetz-Lamour, T. Amthor, S. Westermann, A. de Oliveira, and M. Weidemüller, Coherent excitation of Rydberg atoms in an ultracold gas, Opt. Commun. **264**, 293 (2006).

[9] M. Archimi, C. Simonelli, L. Di Virgilio, A. Greco, M. Ceccanti, E. Arimondo, D. Ciampini, I. I. Ryabtsev, I. I. Beterov, and O. Morsch, Measurements of single-state and state-ensemble lifetimes of high-lying Rb Rydberg levels, Phys. Rev. A **100**, 030501(R) (2019).

[10] J. M. Raimond, P. Goy, M. Gross, C. Fabre, and S. Haroche, Collective Absorption of Blackbody Radiation by Rydberg Atoms in a Cavity: An Experiment on Bose Statistics and Brownian Motion, Phys. Rev. Lett. **49**, 117 (1982).

[11] D. D. Grimes, S. L. Coy, T. J. Barnum, Y. Zhou, S. F. Yelin, and R. W. Field, Direct single-shot observation of millimeter-wave superradiance in Rydberg-Rydberg transitions, Phys. Rev. A **95**, 043818 (2017).

[12] T. Wang, S. F. Yelin, R. Côté, E. E. Eyler, S. M. Farooqi, P. L. Gould, M. Koštrun, D. Tong, and D. Vrinceanu, Superradiance in ultracold Rydberg gases, Phys. Rev. A **75**, 033802 (2007).

[13] K. J. Weatherill, J. D. Pritchard, R. P. Abel, M. G. Bason, A. K. Mohapatra, and C. S. Adams, Electromagnetically induced transparency of an interacting cold Rydberg ensemble, J. Phys. B: At. Mol. Opt. Phys. **41**, 201002 (2008).

[14] J. O. Day, E. Brekke, and T. G. Walker, Dynamics of low-density ultracold Rydberg gases, Phys. Rev. A **77**, 052712 (2008).

[15] L. Hao, Z. Bai, J. Bai, S. Bai, Y. Jiao, G. Huang, J. Zhao, W. Li, and S. Jia, Observation of blackbody radiation enhanced superradiance in ultracold Rydberg gases, New J. Phys. **23**, 083017 (2021).

[16] T. Zhou, B. G. Richards, and R. R. Jones, Absence of collective decay in a cold Rydberg gas, Phys. Rev. A **93**, 033407 (2016).

[17] E. Brekke, J. O. Day, and T. G. Walker, Excitation suppression due to interactions between microwave-dressed Rydberg states, Phys. Rev. A **86**, 033406 (2012).

[18] E. A. Goldschmidt, T. Boulier, R. C. Brown, S. B. Koller, J. T. Young, A. V. Gorshkov, S. L. Rolston, and J. V. Porto, Anomalous Broadening in Driven Dissipative Rydberg Systems, Phys. Rev. Lett. **116**, 113001 (2016).

[19] R. T. Sutherland and F. Robicheaux, Superradiance in inverted multilevel atomic clouds, Phys. Rev. A **95**, 033839 (2017).

[20] R. D. Niederriter, C. Schlupf, and P. Hamilton, Cavity probe for real-time detection of atom dynamics in an optical lattice, Phys. Rev. A **102**, 051301(R) (2020).

[21] T. W. Clark, A. Dombi, F. I. B. Williams, A. Kurko, J. Fortagh, D. Nagy, A. Vukics, and P. Domokos, Time-resolved observation of a dynamical phase transition of atoms in a cavity, arXiv:2106.03544 [quant-ph].

[22] J. Zeiher, J. Wolf, J. A. Isaacs, J. Kohler, and D. M. Stamper-Kurn, Tracking Evaporative Cooling of a Mesoscopic Atomic Quantum Gas in Real Time, Phys. Rev. X **11**, 041017 (2021).

[23] S. Garcia, M. Stammeier, J. Deiglmayr, F. Merkt, and A. Wallraff, Single-Shot Nondestructive Detection of Rydberg-Atom Ensembles by Transmission Measurement of a Microwave Cavity, Phys. Rev. Lett. **123**, 193201 (2019).

[24] B. Huber, T. Baluktsian, M. Schlagmüller, A. Kölle, H. Kübler, R. Löw, and T. Pfau, GHz Rabi Flopping to Rydberg States in Hot Atomic Vapor Cells, Phys. Rev. Lett. **107**, 243001 (2011).

[25] T. Baluktsian, B. Huber, R. Löw, and T. Pfau, Evidence for Strong van der Waals Type Rydberg-Rydberg Interaction in a Thermal Vapor, Phys. Rev. Lett. **110**, 123001 (2013).

[26] Y. Colombe, T. Steinmetz, G. Dubois, F. Linke, D. Hunger, and J. Reichel, Strong atom-field coupling for Bose-Einstein condensates in an optical cavity on a chip, Nature (London) **450**, 272 (2007).

[27] J. Gripp, S. L. Mielke, and L. A. Orozco, Evolution of the vacuum Rabi peaks in a detuned atom-cavity system, Phys. Rev. A **56**, 3262 (1997).

[28] R. Boddeda, I. Usmani, E. Bimbard, A. Grankin, A. Ourjoumtsev, E. Brion, and P. Grangier, Rydberg-induced optical nonlinearities from a cold atomic ensemble trapped inside a cavity, J. Phys. B: At. Mol. Opt. Phys. **49**, 084005 (2016).

[29] J. Sheng, Y. Chao, S. Kumar, H. Fan, J. Sedlacek, and J. P. Shaffer, Intracavity Rydberg-atom electromagnetically induced transparency using a high-finesse optical cavity, Phys. Rev. A **96**, 033813 (2017).

[30] J. Ningyuan, A. Georgakopoulos, A. Ryou, N. Schine, A. Sommer, and J. Simon, Observation and characterization of cavity Rydberg polaritons, Phys. Rev. A **93**, 041802(R) (2016).

[31] M. Fleischhauer, A. Imamoglu, and J. P. Marangos, Electromagnetically induced transparency: Optics in coherent media, Rev. Mod. Phys. **77**, 633 (2005).

[32] E. Brion, L. H. Pedersen, and K. Mølmer, Adiabatic elimination in a lambda system, J. Phys. A: Math. Theor. **40**, 1033 (2007).

[33] N. Šibalić, J. Pritchard, C. Adams, and K. Weatherill, ARC: An open-source library for calculating properties of alkali Rydberg atoms, Comput. Phys. Commun. **220**, 319 (2017).

[34] I. I. Beterov, D. B. Tretyakov, I. I. Ryabtsev, A. Ekers, and N. N. Bezuglov, Ionization of sodium and rubidium nS, nP, and nD Rydberg atoms by blackbody radiation, Phys. Rev. A **75**, 052720 (2007).

[35] R. H. Dicke, Coherence in spontaneous radiation processes, Phys. Rev. **93**, 99 (1954).

[36] V. V. Temnov and U. Woggon, Superradiance and Subradiance in an Inhomogeneously Broadened Ensemble of Two-Level Systems Coupled to a Low-Q Cavity, Phys. Rev. Lett. **95**, 243602 (2005).

[37] M. D. Lukin, M. Fleischhauer, R. Cote, L. M. Duan, D. Jaksch, J. I. Cirac, and P. Zoller, Dipole Blockade and Quantum Information Processing in Mesoscopic Atomic Ensembles, Phys. Rev. Lett. **87**, 037901 (2001).

[38] S. Ravets, H. Labuhn, D. Barredo, T. Lahaye, and A. Browaeys, Measurement of the angular dependence of the dipole-dipole interaction between two individual Rydberg atoms at a Förster resonance, Phys. Rev. A **92**, 020701(R) (2015).